



Universiteit  
Leiden  
The Netherlands

## Rare-Earth-Metal (Nd<sup>3+</sup>, Ce<sup>3+</sup> and Gd<sup>3+</sup>)-Doped CaF<sub>2</sub>: nanoparticles for multimodal imaging in biomedical applications

Yu, Z.F.; He, Y.Y.; Schomann, T.; Wu, K.F.; Hao, Y.; Suidgeest, E.; ... ; Cruz, L.J.

### Citation

Yu, Z. F., He, Y. Y., Schomann, T., Wu, K. F., Hao, Y., Suidgeest, E., ... Cruz, L. J. (2022). Rare-Earth-Metal (Nd<sup>3+</sup>, Ce<sup>3+</sup> and Gd<sup>3+</sup>)-Doped CaF<sub>2</sub>: nanoparticles for multimodal imaging in biomedical applications. *Pharmaceutics*, 14(12).  
doi:10.3390/pharmaceutics14122796

Version: Publisher's Version


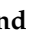
License: [Creative Commons CC BY 4.0 license](#)

Downloaded from: <https://hdl.handle.net/1887/3567456>

**Note:** To cite this publication please use the final published version (if applicable).

## Article

# Rare-Earth-Metal ( $\text{Nd}^{3+}$ , $\text{Ce}^{3+}$ and $\text{Gd}^{3+}$ )-Doped $\text{CaF}_2$ : Nanoparticles for Multimodal Imaging in Biomedical Applications

Zhenfeng Yu <sup>1</sup>, Yuanyuan He <sup>1</sup>, Timo Schomann <sup>1,2</sup>, Kefan Wu <sup>3</sup>, Yang Hao <sup>1</sup>, Ernst Suidgeest <sup>4</sup>, Hong Zhang <sup>3</sup>, Christina Eich <sup>1,\*</sup> and Luis J. Cruz <sup>1,\*</sup>

<sup>1</sup> Translational Nanobiomaterials and Imaging Group, Department of Radiology, Leiden University Medical Center, 2333 ZA Leiden, The Netherlands

<sup>2</sup> Percuros B.V., Zernikedreef 8, 2333 CL Leiden, The Netherlands

<sup>3</sup> Van 't Hoff Institute for Molecular Sciences, University of Amsterdam, Science Park 904, 1098 XH Amsterdam, The Netherlands

<sup>4</sup> C.J. Gorter Center for High Field MRI, Department of Radiology, Leiden University Medical Center, 2333 ZA Leiden, The Netherlands

\* Correspondence: c.eich@lumc.nl (C.E.); l.j.cruz\_ricondo@lumc.nl (L.J.C.)

**Abstract:** Here, we describe the synthesis of a novel type of rare-earth-doped nanoparticles (NPs) for multimodal imaging, by combining the rare-earth elements Ce, Gd and Nd in a crystalline host lattice consisting of  $\text{CaF}_2$  ( $\text{CaF}_2$ : Ce, Gd, Nd).  $\text{CaF}_2$ : Ce, Gd, Nd NPs are small (15–20 nm), of uniform shape and size distribution, and show good biocompatibility and low immunogenicity in vitro. In addition,  $\text{CaF}_2$ : Ce, Gd, Nd NPs possess excellent optical properties.  $\text{CaF}_2$ : Ce, Gd, Nd NPs produce downconversion emissions in the second near-infrared window (NIR-II, 1000–1700 nm) under 808 nm excitation, with a strong emission peak at 1056 nm. Excitation in the first near-infrared window (NIR-I, 700–900 nm) has the advantage of deeper tissue penetration power and reduced autofluorescence, compared to visible light. Thus,  $\text{CaF}_2$ : Ce, Gd, Nd NPs are ideally suited for in vivo fluorescence imaging. In addition, the presence of  $\text{Gd}^{3+}$  makes the NPs intrinsically monitorable by magnetic resonance imaging (MRI). Moreover, next to fluorescence and MR imaging, our results show that  $\text{CaF}_2$ : Ce, Gd, Nd NPs can be used as imaging probes for photoacoustic imaging (PAI) in vitro. Therefore, due to their biocompatibility and suitability as multimodal imaging probes,  $\text{CaF}_2$ : Ce, Gd, Nd NPs exhibit great potential as a traceable imaging agent in biomedical applications.

**Keywords:** multimodal imaging; NIR-II; PAI; MRI; rare-earth-doped nanoparticles



**Citation:** Yu, Z.; He, Y.; Schomann, T.; Wu, K.; Hao, Y.; Suidgeest, E.; Zhang, H.; Eich, C.; Cruz, L.J. Rare-Earth-Metal ( $\text{Nd}^{3+}$ ,  $\text{Ce}^{3+}$  and  $\text{Gd}^{3+}$ )-Doped  $\text{CaF}_2$ : Nanoparticles for Multimodal Imaging in Biomedical Applications.

*Pharmaceutics* **2022**, *14*, 2796. <https://doi.org/10.3390/pharmaceutics14122796>

Academic Editor: Christian Celia

Received: 10 October 2022

Accepted: 8 December 2022

Published: 14 December 2022

Corrected: 12 December 2023

**Publisher's Note:** MDPI stays neutral with regard to jurisdictional claims in published maps and institutional affiliations.



**Copyright:** © 2022 by the authors. Licensee MDPI, Basel, Switzerland. This article is an open access article distributed under the terms and conditions of the Creative Commons Attribution (CC BY) license (<https://creativecommons.org/licenses/by/4.0/>).

## 1. Introduction

Imaging holds a crucial role in the diagnosis of a variety of diseases such as cancer. Early-stage disease diagnosis is important to maximize treatment effects, and to personalize treatments based on the patient's individual variability and medical profile. Molecular imaging techniques provide comprehensive anatomical, physiological and functional information on disease detection and the monitoring of treatment responses. The most commonly used diagnostic imaging methods during the past few decades in the medical field include MRI, X-ray computed tomography (CT) [1], positron emission tomography (PET) [2,3], single-photon emission computed tomography (SPECT) [4], optical fluorescent light imaging (FLI) and photoacoustic imaging (PAI) [5]. Due to differences in their detection methods, spatiotemporal resolution, sensitivity and probe types, the diagnostic information obtained is divergent. Both PET and SPECT use  $\gamma$  rays to detect the in vivo distribution of radioactive tracers to obtain information on biological functions. They have the disadvantages of low spatial resolution, radiation risks and high costs [6–10]. Optical imaging uses visible light and near-infrared probes with different spectral characteristics for molecular and cellular detection but faces several limitations, such as photobleaching, low tissue penetration power, low spatial resolution and autofluorescence [11–15]. While

CT, MRI and PAI can provide structural information, CT detection relies on contrast agents (such as iodine or barium) to obtain images through the different absorption of X-rays by biological tissues, which has the disadvantage of radiation risk and limited soft-tissue resolution [16,17]. MRI, a non-invasive imaging technology uses radio waves (magnetic field), but it has low sensitivity, high cost and scanning and image processing are time-consuming [18–20]. PAI uses high-frequency sound waves (>20 kHz) to generate acoustic energy to detect the difference in echo between chromophores or microbubbles and surrounding tissues in real time. However, due to the limited resolution and sensitivity, the data reproducibility is low, and it cannot provide accurate results [8,21–23]. In summary, to predict and treat diseases more comprehensively and accurately, it is imperative to develop a simple and efficient multifunctional nanomaterial that can integrate multiple imaging modes for detection.

Lanthanides display attractive photophysical properties, such as large anti-Stokes shift, narrow band and multiple emission and long-life luminescence due to their unique  $4f^n$  structure and are widely used in the development of optical probes [24–27].  $\text{Nd}^{3+}$ -doped nanoprobe are downconversion NPs (DCNPs) ranging from NIR-I to NIR-II. They can emit at 890, 1060 and 1340 nm under 808 nm excitation and therefore can be used for near-infrared two-zone imaging [28,29]. Of note, due to the Stokes shift fluorescence mechanism of  $\text{Nd}^{3+}$ ,  $\text{Nd}^{3+}$ -doped NPs have a larger quantum yield than upconversion NPs (UCNPs), and the absorption cross-section of  $\text{Nd}^{3+}$  at 808 nm is larger than the absorption cross-section of  $\text{Yb}^{3+}$  at 980 nm, which leads to little absorption by water molecules at 808 nm when using  $\text{Nd}^{3+}$ -doped nanoprobe. Therefore, compared to  $\text{Yb}^{3+}$ -doped UCNPs, the overheating effect of biological tissues can be more effectively avoided in bioimaging [30]. Because of the many advantages of  $\text{Nd}^{3+}$ ,  $\text{Nd}^{3+}$ -doped NPs are undoubtedly an optical imaging probe with great potential that can be used for biosensing, biological process monitoring and imaging-guided therapy [31].

Another key to obtaining high-quality  $\text{Nd}^{3+}$ -doped nanomaterials is to choose a suitable host matrix material.  $\text{CaF}_2$  is a center-symmetric fluorite crystal with low phonon energy and a wide band gap ( $E_g = 12.1$  eV). It is optically transparent in the wavelength range from ultraviolet to visible light and near infrared, so it is widely used in various types of optical equipment [32–37]. In addition, its unique fluorite structure can be easily doped with lanthanides. Under the condition of not destroying the main configuration, the presence of lanthanides causes internal valence changes and diversified charge compensation, resulting in a lattice structure with rich symmetry. These changes give the lanthanide-doped  $\text{CaF}_2$  crystals strong optical activity in the visible and near-infrared regions [38,39]. Thus,  $\text{CaF}_2$  can be used as an optical matrix material for  $\text{Nd}^{3+}$ -doped nanomaterials.

Since the radius of  $\text{Nd}^{3+}$  is not much different from that of  $\text{Ca}^{2+}$ , trivalent Nd ions replace the crystal sites of divalent Ca ions when they are doped into the  $\text{CaF}_2$  lattice, requiring more  $\text{F}^-$  for charge compensation, but they do not cause obvious crystal changes. However, when the  $\text{Nd}^{3+}$  doping concentration reaches a certain limit,  $\text{Nd}^{3+}$  aggregates and some energy cross-relaxation occurs, which triggers the cluster effect and reduces the luminous efficiency of the nanomaterials [40,41]. In order to overcome this phenomenon, the introduction of optically inactive ions (such as  $\text{Lu}^{3+}$ ,  $\text{Gd}^{3+}$ ,  $\text{Y}^{3+}$ ,  $\text{Yb}^{3+}$ ) can effectively destroy the formation of Nd-Nd clusters, thereby improving the quantum efficiency of the material [42–45]. Notably, the special properties of certain optically inactive ions also offer the possibility of constructing multimodal probes; however, most current multimodal imaging probes are dual-mode probes, and NIR-II-based imaging systems combining more than two modes are still rarely reported, but our previous study demonstrates that triple-mode imaging probes hold great promise for obtaining complementary information. Therefore, we focus on the field of rare-earth triple-mode imaging probes for more exploration [46]. Wang et al. showed that the luminous efficiency of  $\text{CaF}_2$ : Nd co-doped  $\text{Ce}^{3+}$  was 10.4 times higher than that of  $\text{CaF}_2$ : Nd [47]. On the other hand, the seven unpaired electrons of Gd(III) can increase the proton relaxation rate, making  $\text{Gd}^{3+}$  a common contrast agent in MR bioimaging [48,49]. Therefore, we choose  $\text{Ce}^{3+}$ ,  $\text{Gd}^{3+}$  and  $\text{Nd}^{3+}$  co-doping  $\text{CaF}_2$  as the

material in our strategy to construct an imaging mode combining NIR-II imaging with complementary MRI and PAI.

In this study, we used a hydrothermal method to synthesize a citric acid-terminated nanomaterial with  $\text{CaF}_2$  as the matrix, co-doped with the three lanthanide elements—Ce, Gd and Nd. The resulting  $\text{CaF}_2$ : Ce, Gd, Nd NPs had a small particle size, were stable in the presence of serum and showed excellent luminous intensity at 1056 nm. In vitro cell culture experiments demonstrated that  $\text{CaF}_2$ : Ce, Gd, Nd NPs did not induce cellular cytotoxicity and were readily taken up by human breast cancer cells. In addition, the NPs showed low immunogenicity when cultured with antigen-presenting cells, and thus the NPs can be used as a potential imaging probe in vivo. Importantly,  $\text{CaF}_2$ : Ce, Gd, Nd NPs are multimodal and can be detected by NIR-II/PA/MR imaging and therefore provide significant advantages in disease diagnosis. In summary,  $\text{CaF}_2$ : Ce, Gd, Nd NPs represent a novel optical material that can be widely used in the field of medical imaging.

## 2. Materials and Methods

### 2.1. Materials

The following chemicals were acquired from Sigma-Aldrich (St. Louis, MO, USA): neodymium (III) chloride hexahydrate ( $\text{NdCl}_3 \cdot 6\text{H}_2\text{O}$ , 99.9%), calcium chloride dihydrate ( $\text{CaCl}_2 \cdot 2\text{H}_2\text{O}$ , 99.5%), cerium (III) chloride heptahydrate ( $\text{CeCl}_3 \cdot 7\text{H}_2\text{O}$ , 99.9%), potassium citrate tribasic monohydrate ( $\text{HOC}(\text{COOK})(\text{CH}_2\text{COOK})_2 \cdot \text{H}_2\text{O}$ ,  $\geq 99.0\%$ ), gadolinium (III) chloride hexahydrate ( $\text{GdCl}_3 \cdot 6\text{H}_2\text{O}$ , 99.9%), ammonium fluoride ( $\text{NH}_4\text{F}$ ,  $\geq 98.0\%$ ). Biologend (San Diego, CA, USA) supplied the anti-CD40-APC. Thermo Fisher Scientific (Waltham, MA, USA) provided fetal calf serum (FCS), 4',6-Diamidino-2-Phenylindole (DAPI), dulbecco's Modified Eagle's Medium (DMEM) and CD86-FITC. Promega (Madison, WI, USA) offered cell titer 96 Aqueous MTS Reagent Powder. PeproTech (Cranbury, NJ, USA) supplied lipopolysaccharide (LPS). Bioline (London, UK) delivered agarose. Abcam (Cambridge, UK) supplied the phalloidin- iFluor 488 Reagent. All of water used in the experiments was ultrapure deionized water.

### 2.2. Synthesis of the $\text{CaF}_2$ : Ce, Gd, Nd NPs

As previously described [50], we synthesized  $\text{CaF}_2$ : Ce, Gd, Nd NPs by a simple hydrothermal method. Briefly, a total of 3.75 mmol of  $\text{CaCl}_2 \cdot 2\text{H}_2\text{O}$ ,  $\text{CeCl}_3 \cdot 7\text{H}_2\text{O}$ ,  $\text{GdCl}_3 \cdot 6\text{H}_2\text{O}$  and  $\text{NdCl}_3 \cdot 6\text{H}_2\text{O}$  ( $\text{Ca}_{0.98-2x}\text{Ce}_x\text{Gd}_x\text{Nd}_{0.02}\text{F}_{2.02+2x}$ ,  $x = 0.15$ ) were dissolved in 7 mL water and stirred for 10 minutes (min) until fully dissolved. Then, potassium citrate solution was added dropwise to the solution and stirred for 30 min. After that,  $\text{NH}_4\text{F}$  solution was added, and the solution was stirred evenly. The final solution was transferred to a 50 mL Teflon bottle (Baoshishan, China) held in a stainless-steel autoclave, put in an oven (Heraeus, Germany) and maintained at 180 °C for 10 hours (h). Finally, the obtained sample was centrifuged at  $2.4 \times g$  for 20 min and washed three times with water followed by ethanol (99%). The samples were dried in a freeze-dryer (Martin Christ, Osterode, Germany).

The synthesis of  $\text{CaF}_2$ : Nd NPs,  $\text{CaF}_2$ : Ce, Nd NPs,  $\text{CaF}_2$ : Ce, Gd NPs was similar to that of  $\text{CaF}_2$ : Ce, Gd, Nd NPs. The doped concentration of  $\text{Nd}^{3+}$  was maintained at 0.02, and  $\text{Ce}^{3+}$  and  $\text{Gd}^{3+}$  were maintained at 0.15.

### 2.3. Characterization

X-ray diffraction (XRD) analysis of the  $\text{CaF}_2$ : Ce, Gd, Nd NPs was performed by a Panalytical X'pert PRO (Malvern Panalytical, Malvern, UK) operating at a tube voltage of 40 kV and a tube current of 40 mA. The diffraction patterns were acquired using  $\text{Cu K}\alpha$  radiation ( $\lambda = 1.5405 \text{ \AA}$ ) at a scanning rate of  $6.0^\circ/\text{min}$  in the  $2\theta$  range of  $10^\circ \leq 2\theta \leq 70^\circ$ .

The hydrodynamic size and Zeta potential were obtained from  $\text{CaF}_2$ : Ce, Gd, Nd NPs solution (1 mg/mL) using a Malvern ZetaSizer 2000 (Malvern, UK). The analysis software applications were Zetasizer Software (Version 7.13) and GraphPad Prism 8.

IRSpirit FTIR spectrophotometer (Shimadzu, Kyoto, Japan) was used to measure the Fourier transform infrared (FTIR) spectra of  $\text{CaF}_2$ : Ce, Gd, Nd NPs powder. The

spectra were captured in the IRSpirit-TOAPC0027956 mode with a wavenumber range of 600–4000  $\text{cm}^{-1}$  and a resolution of 4  $\text{cm}^{-1}$ . IR Pilot and Origin 8.5 were used for analysis.

The size and morphology of  $\text{CaF}_2$ : Ce, Gd, Nd NPs were examined using a Tecnai 12 Twin transmission electron microscope (TEM) (FEI Company, Hillsboro, OR, USA) outfitted with a OneView Camera Model 1095 (Gatan, Pleasanton, CA, USA) under 120 kV voltage. TEM samples were prepared by pipetting  $\text{CaF}_2$ : Ce, Gd, Nd NPs aqueous solution (1 mg/mL) onto the surface of the copper grid.

$\text{CaF}_2$ : Ce, Gd, Nd NPs were mounted on scanning electron microscopy (SEM) specimen stubs. Then, an Apreo S LoVac SEM (Thermo Scientific, Waltham, MA, USA) equipped with an UltraDry energy-dispersive X-ray spectroscopy (EDS) detector (Thermo Scientific, Waltham, MA, USA) was utilized to analyze the sample. The measurement conditions were: 1500 $\times$  magnification with 30 kV and 51 nA.

A Quantum Design Versalab physical property measurement system with VSM option (Quantum Design, San Diego, CA, USA) was employed to quantify the vibrating-sample magnetometry (VSM) of  $\text{CaF}_2$ : Ce, Gd, Nd NPs (4.51 mg).

The emission spectra of  $\text{CaF}_2$ : Ce, Gd, Nd NPs powder was recorded using Fluorolog<sup>®</sup>-3 with FluoEssence<sup>™</sup> (Horiba, Kyoto, Japan) equipped with a diode laser as the excitation light source, and the emission spectra of  $\text{CaF}_2$ : Nd NPs (powder) and  $\text{CaF}_2$ : Ce, Nd NPs (powder) were recorded using an Edinburgh FLS920 fluorescence spectrometer (Edinburgh Instruments, Edinburgh, UK) with an 808 nm NIR diode laser (300 mW). The absorption spectra of  $\text{CaF}_2$ : Ce, Gd, Nd NPs (10 mg/mL) and  $\text{CaF}_2$ : Ce, Gd NPs (10 mg/mL) were obtained by SpectraMax<sup>®</sup> iD3 Multi-Mode Microplate Reader (Molecular Devices, San Jose, CA, USA). Analysis tool was SoftMax Pro<sup>®</sup> 7 Software.

#### 2.4. Stability of $\text{CaF}_2$ : Ce, Gd, Nd NPs

To assess the stability of  $\text{CaF}_2$ : Ce, Gd, Nd NPs in physiologically relevant buffers, we dissolved  $\text{CaF}_2$ : Ce, Gd, Nd NPs at a concentration of 0.2 mg/mL in 50% FCS solution. The samples were kept in a shaker at 37 °C, and we used a Malvern ZetaSizer 2000 (Malvern, UK) to measure the size and zeta potential at 0 h, 1 d, 2 d, 3 d, 4 d, 5 d, 6 d and 7 d. Data analysis used Zetasizer Software (Version 7.13) and GraphPad Prism 8.

#### 2.5. Hemolysis of $\text{CaF}_2$ : Ce, Gd, Nd NPs

Briefly, a total of 100  $\mu\text{L}$  of fresh blood was collected from the tail vein of BALB/c mice using a vacuum blood collection tube.  $\text{Ca}^{2+}$ / $\text{Mg}^{2+}$ -free PBS was used to dilute the blood 50 times. To extract red blood cells, the blood dilutions were centrifuged at  $0.9 \times g$  for 15 min at 4 °C. The supernatant was removed, and two groups were chosen randomly as negative and positive controls. The negative control group was resuspended with 500  $\mu\text{L}$  of saline, whereas the positive control group was resuspended with 500  $\mu\text{L}$  of 1% Triton X-100 (*v/v*). For the experimental group, blood cells were resuspended with  $\text{CaF}_2$ : Ce, Gd, Nd NPs isotonic saline at five different concentrations (1, 0.5, 0.25, 0.125, 0.0625 mg/mL). The samples were then incubated at 37 °C for 4 h before being centrifuged at  $0.9 \times g$  and 4 °C for 15 min to obtain the supernatant. The absorbance values were measured at 540 nm by an enzyme marker SpectraMax (Molecular Devices, San Jose, CA, USA). The concentration of cytosolic hemoglobin in each sample was assessed according to the hemoglobin concentration standard curve.

The hemolysis ratio was calculated using the hemolysis (HL%) equation follows:

$$H (\text{hemolysis ratio, \%}) = (\text{OD sample} - \text{OD negative}) / (\text{OD positive} - \text{OD negative}) \times 100$$

#### 2.6. MTS Cytotoxicity Assay of $\text{CaF}_2$ : Ce, Gd, Nd NPs

The toxicity of  $\text{CaF}_2$ : Ce, Gd, Nd NPs to cells was assessed by MTS assay using two different cell lines. Briefly, 4T1 cells ( $1 \times 10^4$ ) were seeded in 96 wells and incubated for 24 h at 37 °C. The cells were then treated for 24, 48 and 72 h with varied concentrations of  $\text{CaF}_2$ : Ce, Gd, Nd NPs (0–2000  $\mu\text{g/mL}$ ). Meanwhile, a 96-well plate was inoculated with  $1 \times 10^5$

peripheral blood mononuclear cells (PBMCs)/well, kept in a 37 °C incubator and then incubated with various CaF<sub>2</sub>: Ce, Gd, Nd NPs concentrations (0–125 µg/mL) for 24 h, 48 h and 72 h. Afterwards, the medium was removed and 100 µL of fresh medium and 20 µL of MTS reagent were added to each well as directed by the manufacturer's instructions. The cells were then cultured for 1.5 h at 37 °C in an incubator. The absorbance (OD) was measured using Microplate reader (Molecular Devices, San Jose, CA, USA) at 490 nm. The ratio to the untreated control group was used to assess cell viability. Data are presented as mean ± SD.

### 2.7. Uptake of CaF<sub>2</sub>: Ce, Gd, Nd NPs

Qualitative uptake of CaF<sub>2</sub>: Ce, Gd, Nd NPs in 4T1 cells was determined by confocal microscopy. 4T1 cells were seeded at  $2 \times 10^4$ /well on 13 mm<sup>3</sup> circular coverslips in 24-well plates. After 24 h, 4T1 cells were co-incubated with 250 µg/mL of CaF<sub>2</sub>: Ce, Gd, Nd NPs medium at 37 °C for 1, 4, 24 and 48 h. Cells treated with medium without NPs served as a control group. At the end of the incubation time, the cells were washed 5 times with PBS to remove the unabsorbed NPs. At room temperature, the cells were fixed with 4% paraformaldehyde for 15 min, washed twice with PBS, treated with 0.1% Triton PBS for 10 min and washed 3 times with PBS. Finally, cell nuclei were labeled with DAPI for 5 min. After washing with PBS, coverslips were sealed on slides with fluorCare sealer. The slides were imaged using a SP8 LIGHTNING Confocal Microscope (Leica Biosystems Nussloch GmbH, Germany) and analyzed by LAS X (Leica Application Suite X) software.

### 2.8. In Vitro Dendritic Cell (DC) Activation Study

In order to evaluate the effect of CaF<sub>2</sub>: Ce, Gd, Nd NPs on immune cells, we used flow cytometry to assess the expression of DC maturation/activation markers. Briefly, murine D1 DCs and 125 µg/mL CaF<sub>2</sub>: Ce, Gd, Nd NPs were co-cultured in a 96-well plate for 24 h in a 37 °C incubator. PBS/EDTA (Sigma-Aldrich, St. Louis, MO, USA) was used to detach the cells, which were then washed with FACS buffer and stained with anti-CD40-APC (Biolegend, San Diego, CA, USA) and anti-CD86-FITC (eBioscience, San Diego, CA, USA) antibodies. The cells were washed and resuspended in 100 µL FACS buffer after 30 min. A LSR-II cytometer (BD Biosciences, Franklin Lakes, NJ, USA) was used to measure the samples, and FlowJo (version 10) was utilized to analyze the data.

### 2.9. Multimodal Imaging Properties of CaF<sub>2</sub>: Ce, Gd, Nd NPs

#### 2.9.1. NIR-II imaging

We employed an in vivo NIR-II optical imaging system (Kaer Labs, Nantes, France) to evaluate the NIR-II imaging capabilities of our NPs. CaF<sub>2</sub>: Ce, Gd, Nd NPs were suspended in ddH<sub>2</sub>O at 2 mg/mL, while the InGaAs camera was chilled to −20 °C at mid-gain setup. We obtained photos at various wavelengths using an 808 nm laser excitation at 50 mW/cm<sup>2</sup>. Images were recorded with the KIS NIR-II system.

#### 2.9.2. Photoacoustic Imaging

The PA and B-mode ultrasound images were acquired using Vevo LAZR-X (FUJIFILM VisualSonics, Toronto, ON, Canada), and a MX550D transducer was utilized. CaF<sub>2</sub>: Ce, Gd, Nd NP solution was injected into an 0.5% agarose gel. The experiment was carried out with the center transmit of 40 MHz and the axial resolution of 40 µm. Vevo LAB 5.5.0 was used to analyze the data.

#### 2.9.3. MRI Studies

MRI studies were carried out using a 7T Bruker BioSpec (Ettlingen, Germany), and ParaVision 360 (Version 2.0. pl.1) software was used to analyze attenuation images. CaF<sub>2</sub>: Ce, Gd, Nd NPs were dissolved in 1% agarose solution, and the concentrations were 0 mg/mL, 1 mg/mL, 2 mg/mL, 3 mg/mL, 4 mg/mL and 5 mg/mL. The microwave oven was used to heat the solutions and create the gel sample. T<sub>1</sub> relaxation was assessed using

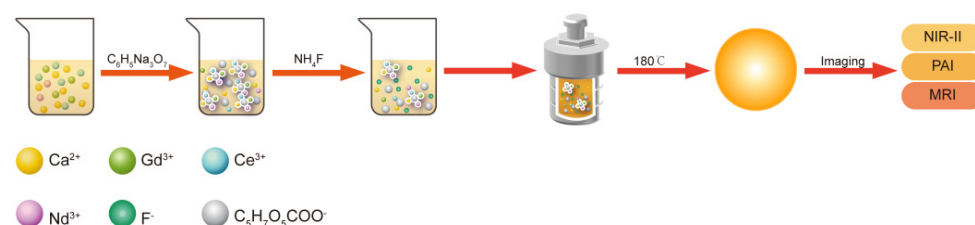
a saturation recovery sequence and the parameters were as follows: repetition times (TR) array = 18, 35, 70, 125, 250, 500, 1050, 2250, 4500, 9000 ms; echo time (TE) = 6 ms; matrix size (MTX) =  $64 \times 64$ ; field of view (FoV) =  $30 \times 30 \text{ mm}^2$ ; slice thickness (SL) = 2 mm.  $T_2$  relaxation was measured using a multi spin echo sequence and the parameters were as follows: TR = 2200 ms; TE = 6.5 ms; echo spacing = 25 echoes; MTX =  $64 \times 64$ ; FoV =  $30 \times 30 \text{ mm}^2$  and SL = 2 mm. To investigate the MRI characteristics of NPs under biological conditions, we fixed C57BL/6J mouse cadavers after subcutaneously injecting 100  $\mu\text{L}$  of  $\text{CaF}_2$ : Ce, Gd, Nd NPs (10 mg/mL) and took MR images before and after the injection. The measurement conditions were gradient echo sequence with TR/TE = 10/2.8 ms, FoV =  $40 \times 40 \text{ mm}^2$ , matrix =  $256 \times 256$ . The MRI data were acquired using ParaVision 360 (Version 2.0. pl.1, Bruker, Germany) software. Standard mono-exponential functions were used to calculate relaxation times.

### 2.10. Statistical Analysis

The statistical tests performed by GraphPad Prism software 8 (GraphPad Software, San Diego, CA, USA). Statistical differences were considered significant at \*  $p < 0.05$ , \*\*  $p < 0.01$ , \*\*\*  $p < 0.001$  and \*\*\*\*  $p < 0.0001$ .

## 3. Results and Discussion

To explore whether our strategy of synthesizing a multimodal citric acid-terminated nanomaterial with  $\text{CaF}_2$  as the matrix, co-doped with the three lanthanide elements—Ce, Gd and Nd—was feasible, we adapted a previously published hydrothermal method to obtain  $\text{Yb}^{3+}/\text{Tm}^{3+}$ -doped  $\text{MF}_2$  (M = Ca, Sr) colloids to synthesize  $\text{CaF}_2$ : Ce, Gd, Nd. Briefly,  $\text{Ca}^{2+}$ ,  $\text{Ce}^{3+}$ ,  $\text{Gd}^{3+}$ ,  $\text{Nd}^{3+}$  were dissolved in water. Next, solutions of potassium citrate tribasic monohydrate and  $\text{NH}_4\text{F}$  were added in turn to obtain the final solution. The resulting solution was heated in an oven (Heraeus, Germany) at  $180^\circ\text{C}$  for 10 h to synthesize NPs. The obtained sample was centrifuged, washed and freeze-dried (Scheme 1). The physicochemical properties of the synthesized NPs were carefully characterized.



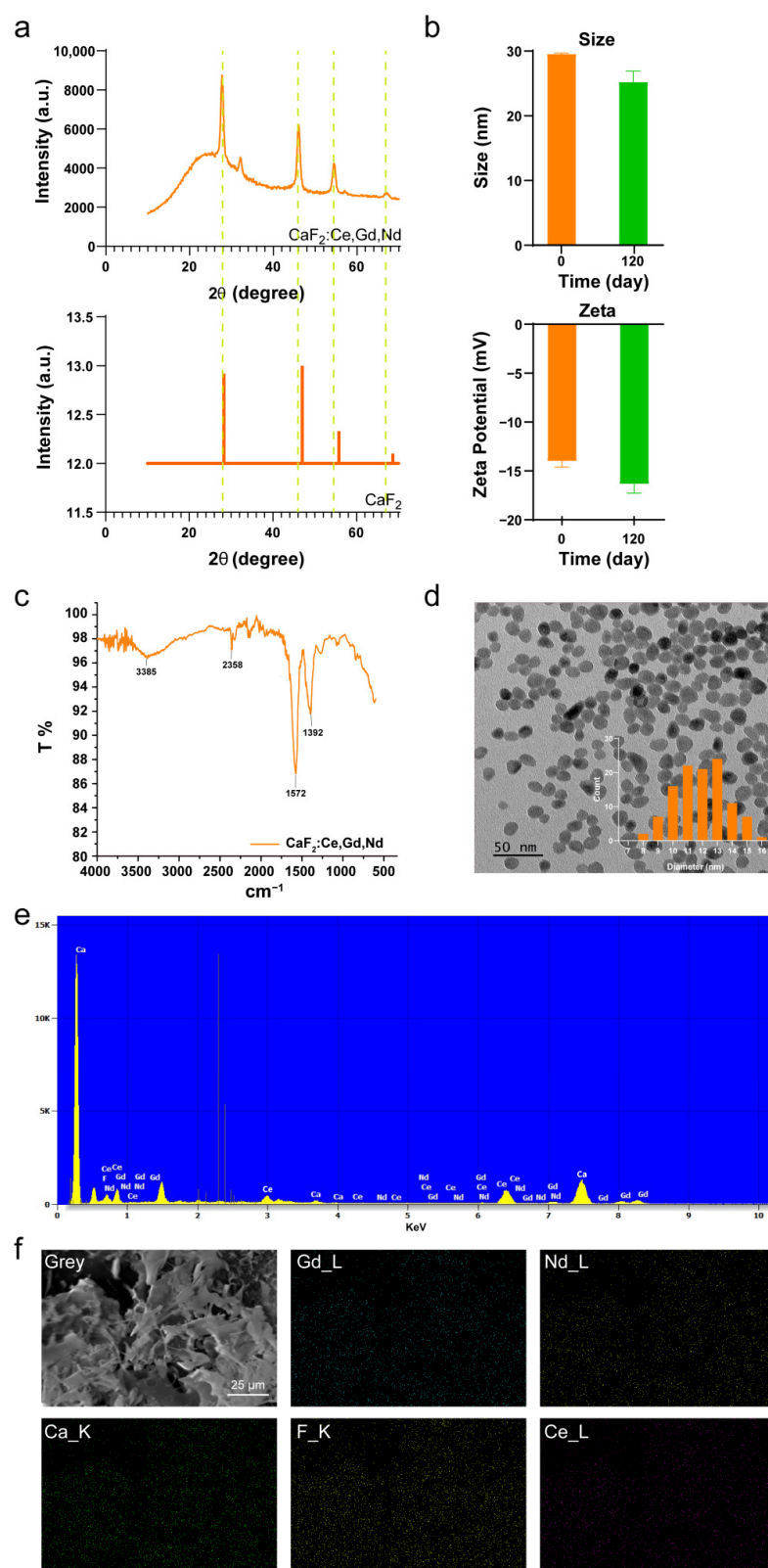
**Scheme 1.** Synthesis process and applications of  $\text{CaF}_2$ : Ce, Gd, Nd NPs.

First, to confirm that the main matrix of the synthesized NPs consisted of  $\text{CaF}_2$ , we performed an XRD analysis (Figure 1a). Through XRD pattern analysis, it can be seen that the main diffraction peaks of  $\text{CaF}_2$ : Ce, Gd, Nd powder correspond to the  $\text{CaF}_2$  crystal standard card, and the addition of  $\text{Ce}^{3+}$ ,  $\text{Gd}^{3+}$ ,  $\text{Nd}^{3+}$  did not change the  $\text{CaF}_2$  cubic phase structure but only resulted in a slight shift of diffraction peaks (Figure 1a). This is because the trivalent lanthanide ions replaced  $\text{Ca}^{2+}$ , which resulted in Ca vacancies and exhibited lattice defects. Moreover, due to the differences in ionic radius and valence, the excess of positive charge needed more  $\text{F}^-$  to compensate, which changed the bond length and reduced the symmetry of the crystal [51]. In addition, a small peak appeared at about  $30^\circ$ , which has been demonstrated to correspond to the doping of rare-earth elements [52,53]. This also confirmed the successful doping of  $\text{Ce}^{3+}$ ,  $\text{Gd}^{3+}$ ,  $\text{Nd}^{3+}$  into the  $\text{CaF}_2$  crystal. DLS data showed that the NPs had a relatively stable particle size of  $29.53 \pm 0.16 \text{ nm}$  in water. Zeta potential measurement showed that the NPs had a negative surface charge of  $-16.6 \pm 0.75 \text{ mV}$ . This is because sodium citrate was used as a complexing agent during NPs synthesis, and as a result, the NPs surface harbors carboxyl groups. The carboxyl group of citrate is negatively charged in water, and the electrostatic repulsion is the reason why  $\text{CaF}_2$ : Ce, Gd, Nd NPs are stable in solution. To examine the stability and shelf-life

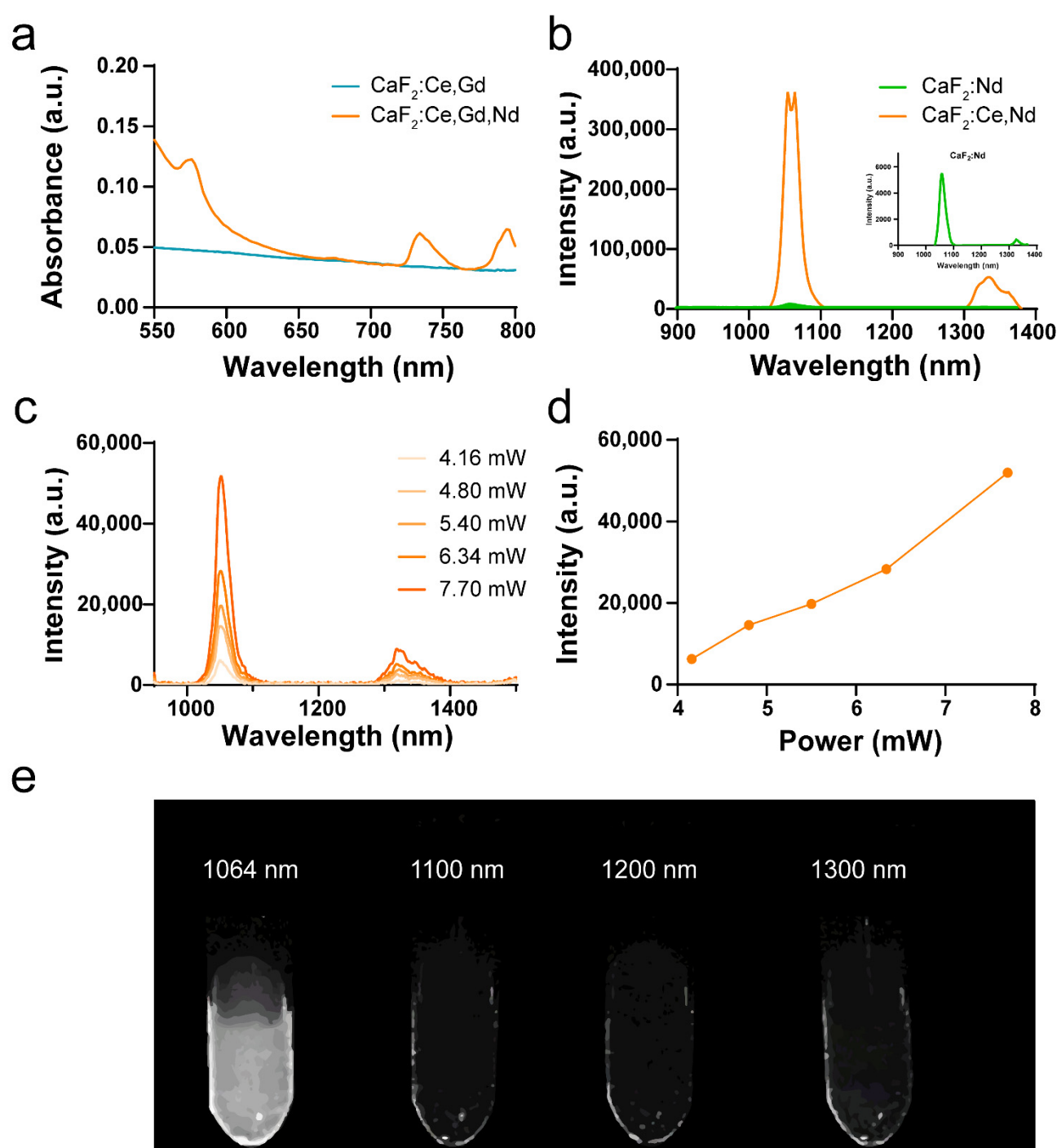
of  $\text{CaF}_2$ : Ce, Gd, Nd NPs, we repeated the DLS measurement after storing the NPs for 4 months at room temperature (Figure 1b). There was no significant change in the particle size and zeta potential of the NPs, suggesting that  $\text{CaF}_2$ : Ce, Gd, Nd NPs show excellent shelf-life stability.  $\text{CaF}_2$ : Ce, Gd, Nd NPs have two main absorption peaks at 1392 and  $1572\text{ cm}^{-1}$ , which correspond to the sodium citrate bands (Figure 1c). On the other hand, the absorption peaks, indicating that the carboxyl groups were conjugated to the metal ion on the surface of the NPs. Therefore, FTIR effectively proved the presence of citrate anions on the surface of the  $\text{CaF}_2$ : Ce, Gd, Nd NPs [54]. In order to study the morphology of  $\text{CaF}_2$ : Ce, Gd, Nd NPs more accurately, we performed a TEM analysis (Figure 1d). The TEM results showed that the NPs have a uniform and stable morphology, about 12 nm, which met our expectations. The discrepancy between the DLS and TEM results on particle size is due to the fact that the DLS measures the hydrodynamic diameter, while the TEM measures the hard boundary [55]. Additionally, to further investigate the elemental composition of the  $\text{CaF}_2$ : Ce, Gd, Nd NPs, we performed EDS on powdered NPs. In Figure 1e, we can see that the strongest peak corresponds to Ca, the smaller peaks to F, Ce and Gd and the weakest peak to Nd. We did not detect any impurity peaks. This result is consistent with the proportion of doped elements in our synthesis process. In addition, mapping results revealed signals for all these elements, and the distribution is homogeneous (Figure 1f). In summary, these results prove that the rare-earth ions ( $\text{Ce}^{3+}$ ,  $\text{Gd}^{3+}$ ,  $\text{Nd}^{3+}$ ) have been successfully doped into  $\text{CaF}_2$ .

In order to evaluate the optical properties of the NPs, we first measured the absorption spectra of the  $\text{CaF}_2$ : Ce, Gd, Nd NPs and  $\text{CaF}_2$ : Ce, Gd NPs in aqueous solution at a concentration of 10 mg/mL (Figure 2a). Compared to  $\text{CaF}_2$ : Ce, Gd NPs, the  $\text{CaF}_2$ : Ce, Gd, Nd NPs showed absorption peaks at 576 nm, 734 nm and 795 nm, corresponding to the  $^4\text{G}_{5/2} + ^2\text{G}_{7/2}$ ,  $^4\text{F}_{7/2} + ^4\text{S}_{3/2}$ , and  $^4\text{F}_{5/2} + ^2\text{H}_{9/2}$  absorption peaks of  $\text{Nd}^{3+}$  [45,56]. Then, to demonstrate that the doping of Ce increased the luminescence intensity of the NPs, we first tested the luminescence intensity of  $\text{CaF}_2$ : Nd and  $\text{CaF}_2$ : Ce, Nd under 808 nm laser excitation (300 mW) (Figure 2b). The experimental results demonstrated that the doping of Ce significantly increased the luminescence intensity of the NPs, and this result was consistent with the results of Wang et al. [47]. Next, we measured the luminescence intensity of the NP sample under increasing laser powers at an excitation wavelength of 808 nm (Figure 2c). The NPs showed a strong signal in the near-infrared region, with two main emission peaks at 1056 nm and 1340 nm, corresponding to the  $^4\text{F}_{3/2} \rightarrow ^4\text{I}_{11/2}$  and  $^4\text{F}_{3/2} \rightarrow ^4\text{I}_{13/2}$  electronic transitions of  $\text{Nd}^{3+}$ , respectively [57–59]. The strongest emission peak was observed at 1056 nm, when the laser power reached 7.7 mW, and an intensity of about  $5 \times 10^4$ , which proves its unique NIR-II efficiency (Figure 2d). On the other hand, since  $\text{Nd}^{3+}$  is the main emission center of the NPs, under 808 nm laser excitation,  $\text{CaF}_2$ : Ce, Gd, Nd NPs can effectively reduce the biological tissue damage during the application process, especially the overheating effect caused by the laser. Moreover, the  $\text{Nd}^{3+}$  emission spectra were located in the second near-infrared window (1000–1400 nm), resulting in a deeper penetration depth and smaller autofluorescence effect of the NPs [52]. Based on the above generated data, an NIR-II system was employed to evaluate the NIR-II imaging properties of  $\text{CaF}_2$ : Ce, Gd, Nd NPs (Figure 2e). Under 808 nm laser excitation,  $\text{CaF}_2$ : Ce, Gd, Nd NPs showed near-infrared emission at 1064 nm. This result is consistent with the  $^4\text{F}_{3/2} \rightarrow ^4\text{I}_{11/2}$  energy transition of  $\text{Nd}^{3+}$ , which proves that the main emission center is  $\text{Nd}^{3+}$ . Thus, our data confirms that  $\text{CaF}_2$ : Ce, Gd, Nd NPs are suitable NIR-II imaging probes.

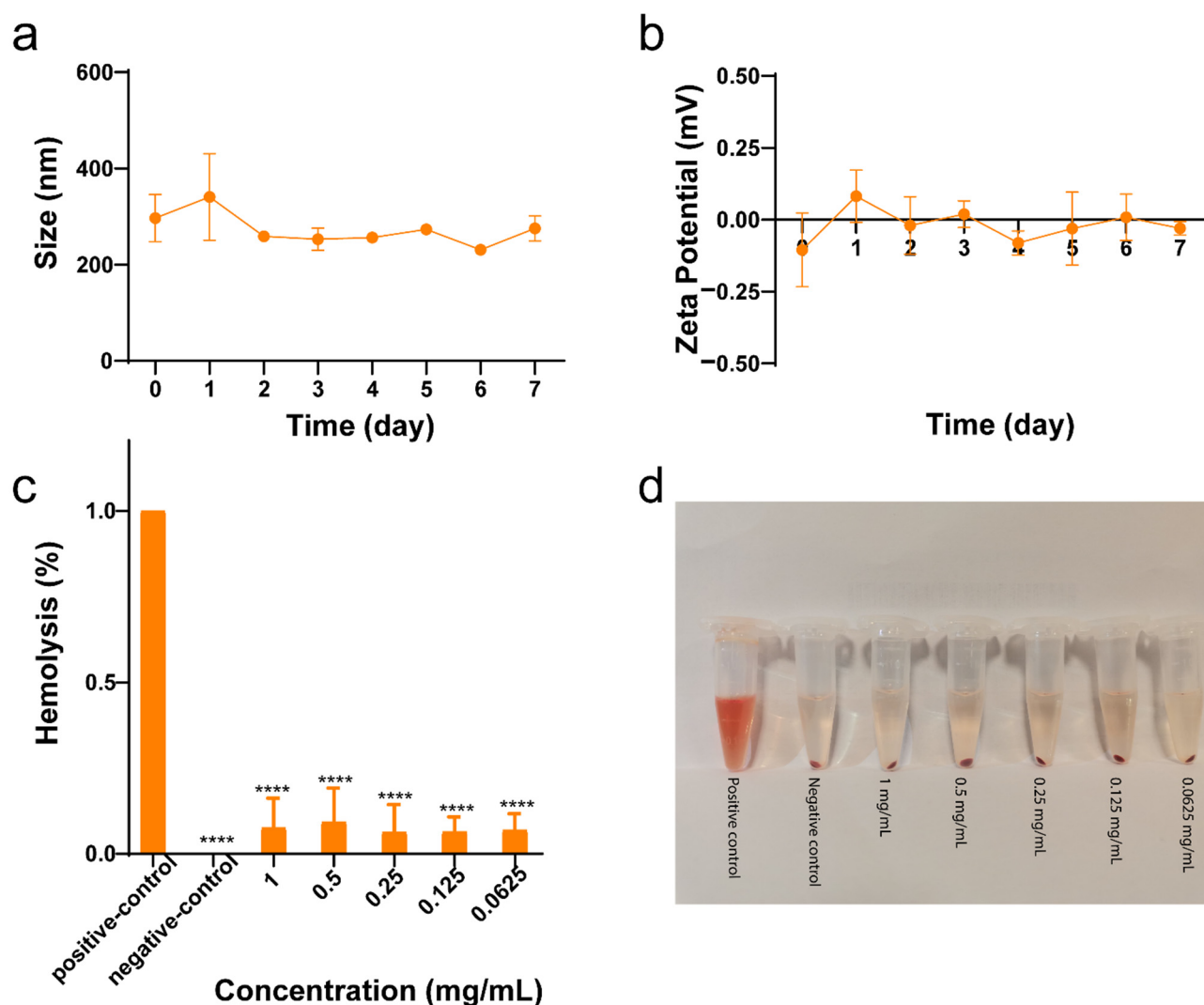
Good colloidal stability is one of the prerequisites for judging whether NPs can be used in biological applications. In order to determine whether  $\text{CaF}_2$ : Ce, Gd, Nd NPs have good colloidal stability, the NPs were redispersed in NaCl containing 50% FCS, and then the particles were measured repeatedly (three times) using a Malvern ZetaSizer 2000 (Malvern, UK) at different time periods to determine the particle size. The results showed that there was no significant change in the size and zeta potential of the NPs in 50% FCS (Figure 3a,b). This demonstrates that the NPs exhibit a relatively stable state when 50% FCS was added to NaCl.



**Figure 1.** Morphology of  $\text{CaF}_2:\text{Ce,Gd,Nd}$  NPs. (a) XRD images of  $\text{CaF}_2:\text{Ce,Gd,Nd}$  NPs and  $\text{CaF}_2$ ; (b) DLS image of  $\text{CaF}_2:\text{Ce,Gd,Nd}$  NPs at 0 d and 120 d; (c) FTIR image of  $\text{CaF}_2:\text{Ce,Gd,Nd}$  NPs; (d) TEM images of  $\text{CaF}_2:\text{Ce,Gd,Nd}$  NPs, where the inset shows the size distribution of  $\text{CaF}_2:\text{Ce,Gd,Nd}$  NPs; (e) EDS spectrum of  $\text{CaF}_2:\text{Ce,Gd,Nd}$  NPs; (f) mapping images of  $\text{CaF}_2:\text{Ce,Gd,Nd}$  NPs.



**Figure 2.** Optical properties of  $\text{CaF}_2$ : Ce, Gd, Nd NPs. (a) The absorption spectra of  $\text{CaF}_2$ : Ce, Gd, Nd NPs solution and  $\text{CaF}_2$ : Ce, Gd NPs (10 mg/mL) measured with SpectraMax<sup>®</sup> iD3 Multi-Mode Microplate Reader; (b) emission spectra of  $\text{CaF}_2$ : Nd NPs and  $\text{CaF}_2$ : Ce, Nd NPs (powder) measured with Edinburgh FLS920 fluorescence spectrometer with an 808 nm NIR diode laser (300 mW), where the inset shows a zoomed-in spectra of  $\text{CaF}_2$ : Nd NPs; (c) emission spectra of  $\text{CaF}_2$ : Ce, Gd, Nd NPs under 808 nm laser excitation; (d) the emission intensities of  $\text{CaF}_2$ : Ce, Gd, Nd-NPs at different laser powers (excited by an 808 nm laser); (e) NIR-II images of  $\text{CaF}_2$ : Ce, Gd, Nd NPs (2 mg/mL) at different wavelengths (excited by an 808 nm laser, 50 mW/cm<sup>2</sup>).

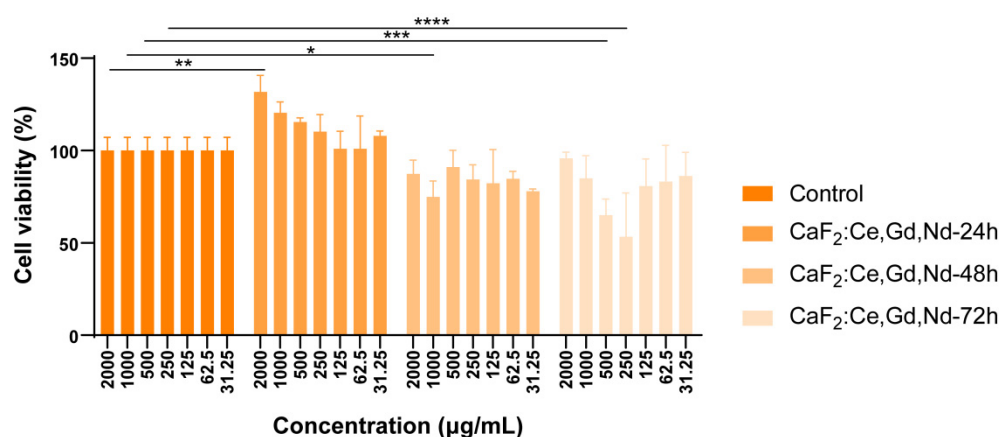


**Figure 3.** Stability of CaF<sub>2</sub>: Ce, Gd, Nd NPs. (a) Size of CaF<sub>2</sub>: Ce, Gd, Nd NPs in 50% FCS; (b) Zeta potential of CaF<sub>2</sub>: Ce, Gd, Nd NPs in 50% FCS; (c) hemolysis of CaF<sub>2</sub>: Ce, Gd, Nd NPs after incubation with red blood cells at multiple concentrations (0–1 mg/mL) for 4 h, with PBS and deionized water serving as negative and positive controls, respectively; (d) hemolysis photo after centrifugation. All data presented the mean values  $\pm$  SD from three independent trials. By comparing experimental groups to control group, one-way ANOVA was used to determine statistical significance (\*\*\*\*  $p < 0.0001$ ).

To evaluate the NPs' biocompatibility with blood components, the effect of CaF<sub>2</sub>: Ce, Gd, Nd NPs on red blood cell (RBC) hemolysis was studied. To this end, murine peripheral blood cells were incubated at 37 °C for 4 h with different concentrations of CaF<sub>2</sub>: Ce, Gd, Nd NPs, and the hemolysis rate of the NPs was calculated by comparing the absorbance ( $\lambda = 540$  nm) of the samples with the positive (1% Triton X-100) and negative (saline) controls [60] (Figure 3c,d). At the highest concentration (1 mg/mL), the hemolysis rate was calculated to be 0.08%, which is negligible. Thus, our results show that CaF<sub>2</sub>: Ce, Gd, Nd NPs have excellent blood compatibility and can be used for intravenous in vivo imaging.

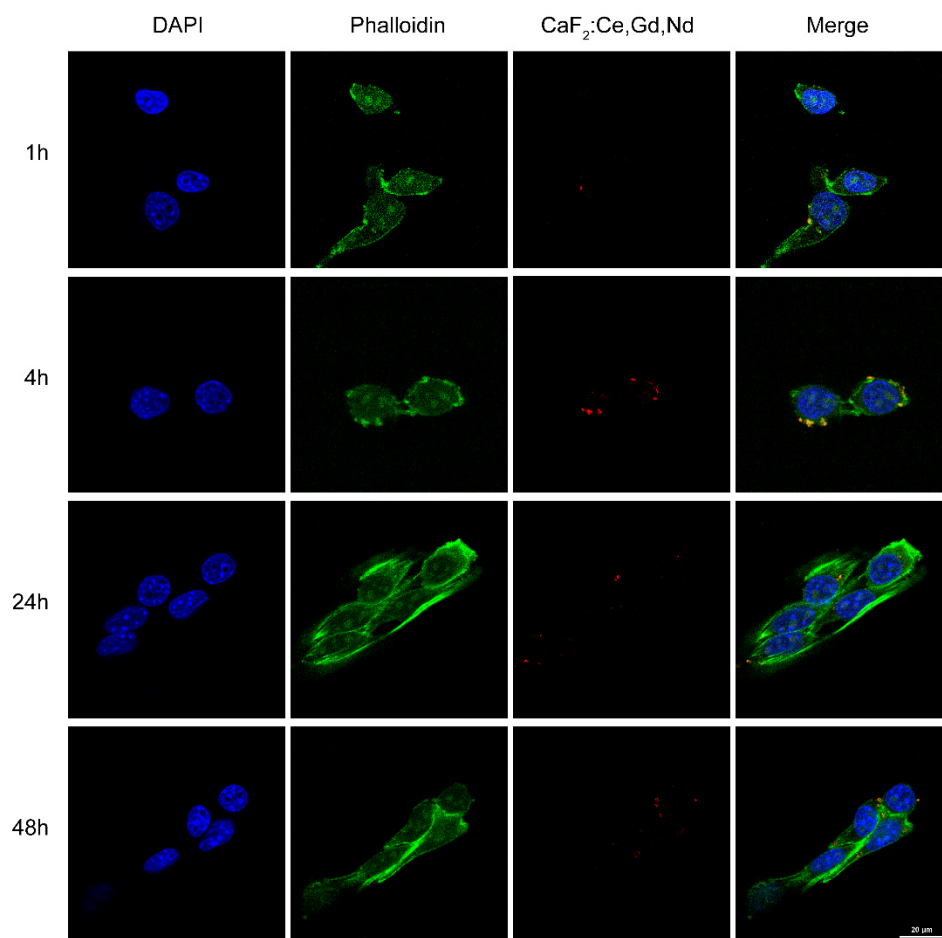
To determine whether the NPs induce cellular toxicity, the effect of CaF<sub>2</sub>: Ce, Gd, Nd NPs on the viability of 4T1 cells was measured by MTS assay (Figure 4). 4T1 is a highly tumorigenic and aggressive breast cancer cell line which grows and spreads metastatically, similar to human breast cancer, and is used as a typical cell model for cancer studies. 4T1 cells were cultured in the presence of different concentrations of CaF<sub>2</sub>: Ce, Gd, Nd NPs for 24 h, 48 h and 72 h. At 24 h, CaF<sub>2</sub>: Ce, Gd, Nd NPs below

1000 µg/mL had no significant effect on the viability of 4T1 cells ( $p > 0.05$ ). Cell viability was significantly higher at a concentration of 2000 µg/mL ( $** p < 0.01$ ). Values higher than 100% indicate that the NPs may have a positive effect on cell proliferation [61]. Secondly, CaF<sub>2</sub>: Ce, Gd, Nd NPs contain citric acid groups on the surface, which may participate in the intracellular tricarboxylic acid cycle reaction, resulting in increased cell activity. At 48 h, cell viability was significantly reduced by 15% when the concentration of CaF<sub>2</sub>: Ce, Gd, Nd NPs was 1000 µg/mL compared to the control ( $* p < 0.05$ ). At 72 h, the doses of 500 and 250 µg/mL CaF<sub>2</sub>: Ce, Gd, Nd NPs showed a significant inhibitory trend on 4T1 cells ( $*** p < 0.001$ ,  $**** p < 0.0001$ ). There was no difference between the cell survival rates when the concentration was  $< 125$  µg/mL compared to the control group ( $p > 0.05$ ). As cancer cell lines show biological differences compared to normal, healthy cells, we also tested the effect of CaF<sub>2</sub>: Ce, Gd, Nd NPs (0–125 µg/mL) on the viability of human peripheral blood mononuclear cells (PBMCs). As shown in Figure S1, there was no significant cytotoxic effect of the NPs on cell activity at 24 h and 48 h after NP incubation compared to the control group. Thus, CaF<sub>2</sub>: Ce, Gd, Nd NPs show great promise for biological applications, but further studies are needed to determine the optimal concentration and potential cytotoxic effects.



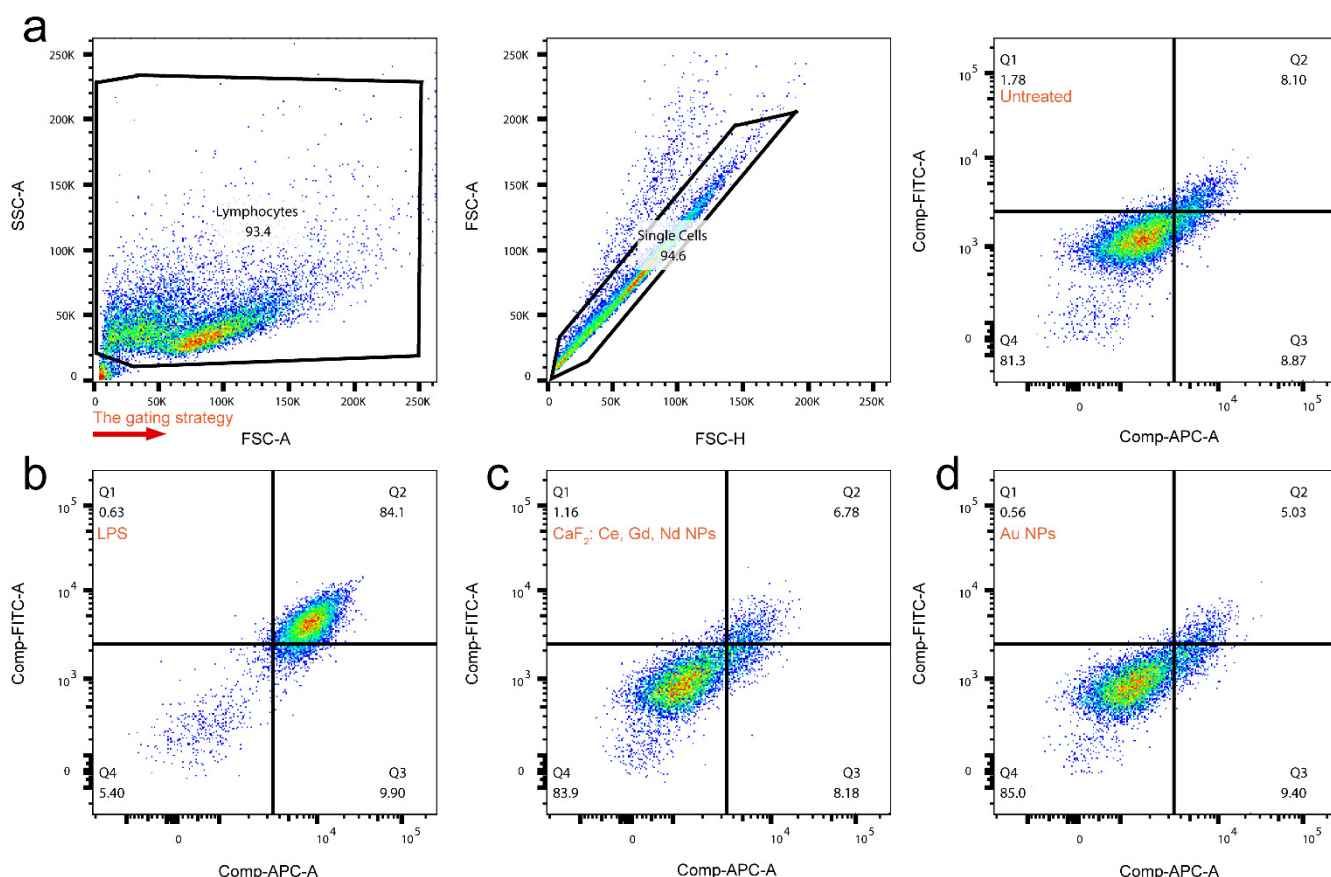
**Figure 4.** Cell viability. 4T1 cells were treated with CaF<sub>2</sub>: Ce, Gd, Nd NPs at varying concentrations (0–2000 µg/mL) for 24 h, 48 h and 72 h. Data represent the mean values  $\pm$  SD from three independent experiments. Statistical significance was calculated using two-way ANOVA, by comparing experimental groups to control group ( $* p < 0.05$ ,  $** p < 0.01$ ,  $*** p < 0.001$  and  $**** p < 0.0001$ ).

We further investigated the uptake potential of CaF<sub>2</sub>: Ce, Gd, Nd NPs by murine breast cancer cells. As demonstrated in Figure 2a, optical characteristics of CaF<sub>2</sub>: Ce, Gd, Nd NPs overlap with the excitation and emission spectra of commonly employed dyes in flow cytometry and microscopy applications, such as Alexa Fluor 568. Thus, we reasoned that our NPs might be inherently monitorable by confocal microscopy. In order to determine the NP uptake rate and intracellular localization of NPs in 4T1 cells, we performed a confocal analysis (Figure 5). To this end, 4T1 cells were incubated with 250 µg/mL CaF<sub>2</sub>: Ce, Gd, Nd NPs (red) at 37 °C for 1 h, 4 h, 24 h and 48 h, followed by co-labeling with DAPI (blue) to stain the nucleus and phalloidin (green) to stain the actin cytoskeleton. Visual inspection confirmed that CaF<sub>2</sub>: Ce, Gd, Nd NPs could be effectively visualized as distinct dots by confocal microscopy. After 1 h co-incubation, few NPs were found attached to the cell membrane. With increasing incubation time, more red fluorescent dots were found in the cytoplasm, indicating that more NPs entered the cells (Figure 5). Based on the above results, we conclude that CaF<sub>2</sub>: Ce, Gd, Nd NPs were effectively taken up by 4T1 cancer cells.



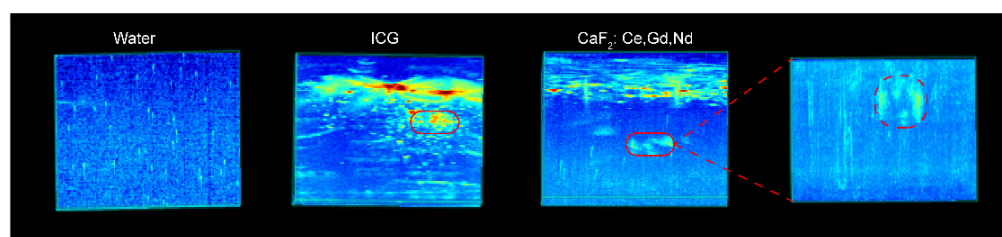
**Figure 5.** Uptake of  $\text{CaF}_2$ : Ce, Gd, Nd NPs by 4T1 cells. Representative confocal microscopy images showing the uptake of  $\text{CaF}_2$ : Ce, Gd, Nd NPs after 1 h, 4 h, 24 h and 48 h of incubation at 37 °C. Cell nuclei (blue), actin cytoskeleton (green),  $\text{CaF}_2$ : Ce, Gd, Nd NPs (red). Scale bar = 20  $\mu\text{m}$ .

Next, we determined whether  $\text{CaF}_2$ : Ce, Gd, Nd NPs, without further modification, can activate the immune system, which could cause adverse side effects in vivo. Previous studies have shown that when immature dendritic cells (DCs) encounter various activation stimuli, they will mature and increase the expression of costimulatory markers on their surface [62–64]. Therefore, we cultured murine immature D1DCs in the presence of  $\text{CaF}_2$ : Ce, Gd, Nd NPs for 24 h and assessed the expression of the DC costimulatory receptors CD86 and CD40 by flow cytometry. As positive control for DC maturation, we included D1 cells that were treated with LPS. After duplicate exclusion, the expression of CD86 and CD40 was analyzed on single D1 cells (Figure 6a). In the non-treated control group, 8% of the cells were double positive for CD86 and CD40 (Figure 6a), and the expression increased to 84% when the cells were treated with LPS (Figure 6b). When D1 cells were treated with a high concentration of  $\text{CaF}_2$ : Ce, Gd, Nd NPs (125  $\mu\text{g}/\text{mL}$ ), 7% of the cells co-expressed CD86 and CD40 (Figure 6c), similar to the levels in the controls group, and in a negative controls group, where Au NPs were added that are known to be non-immunogenic (Figure 6d). In summary, these data indicate that  $\text{CaF}_2$ : Ce, Gd, Nd NPs are inert and do not induce immune activation.



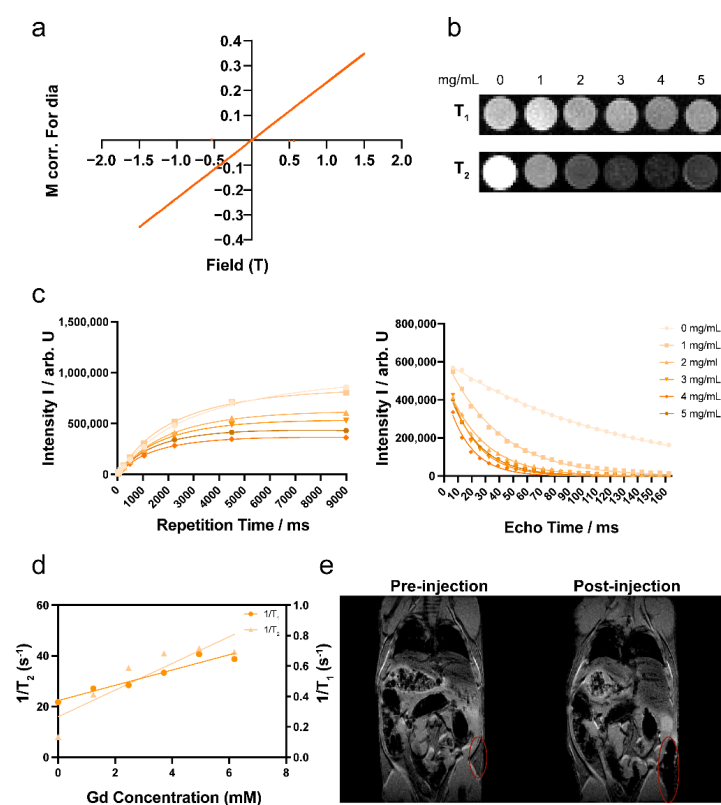
**Figure 6.** In vitro D1DC activation of  $\text{CaF}_2$ : Ce, Gd, Nd NPs measured with FACS flow cytometry. D1DCs were incubated with samples for 24 h. (a) Gating strategy of D1DCs; (b) LPS (1  $\mu\text{g/mL}$ ) incubate with D1DCs as the positive control; (c)  $\text{CaF}_2$ : Ce, Gd, Nd NPs (125  $\mu\text{g/mL}$ ) incubate with D1DCs; (d) Au NPs (125  $\mu\text{g/mL}$ ) incubate with D1DCs as the negative control.

Yang et al. have shown that rare-earth-doped particles can be employed as PAI agents [65]. Furthermore, since PAI is an imaging method that combines light excitation and ultrasound technology, the multiple absorption peaks of rare-earth NPs provide an opportunity as a PAI contrast agent. In order to determine whether  $\text{CaF}_2$ : Ce, Gd, Nd NPs are suitable for ultrasound imaging, we placed the NPs into an agarose phantom, mimicking biological tissue, for imaging by PA (Figure 7). In this gel phantom, the NPs showed PA signals at 808 nm wavelength, which was stronger than in the control agarose without NPs, but slightly dimmer than in the ICG group, a dye that is well suited for PAI. When the NPs were irradiated by the laser, part of the light energy was absorbed and converted into heat energy, which caused thermoelastic expansion and generated the PA signal. It effectively proves that  $\text{CaF}_2$ : Ce, Gd, Nd NPs have the ability to serve as NIR-II and PA probes.



**Figure 7.** In vitro PA images of  $\text{CaF}_2$ : Ce, Gd, Nd NPs (5  $\text{mg/mL}$ ) in the agarose gel.

Since  $\text{Gd}^{3+}$  chelating material is a common “positive” clinical MRI contrast agent, we inferred that  $\text{CaF}_2$ : Ce, Gd, Nd NPs might be suitable as imaging probes for MRI. The magnetic properties of  $\text{CaF}_2$ : Ce, Gd, Nd NPs were first verified using VSM. At room temperature (300 K) and an applied magnetic field of 1.5 T, we noticed that the NPs enhance their magnetic properties as the magnetic field increases, showing a typical paramagnetic behavior consistent with the magnetic characteristics of Gd ions (Figure 8a). The diamagnetic contribution was calculated to be  $0.0032 \text{ Am}^2/\text{kg}$  [66,67]. In order to prove the hypothesis that  $\text{CaF}_2$ : Ce, Gd, Nd NPs can be used as an MRI probe, we mixed  $\text{CaF}_2$ : Ce, Gd, Nd NPs with agarose gel and performed an MRI measurement. Figure 8b shows that as the concentration of NPs increased, the  $T_2$ -weighted MR image became darker; in this concentration range the visually observable contrast in  $T_1$ -weighted MR images was much smaller. We investigated the MRI properties of the NPs by testing the longitudinal magnetization recovery and the transverse magnetization decay (Figure 8c). We plotted the  $R_1$  ( $1/T_1$ ) and  $R_2$  ( $1/T_2$ ) relaxation rates, the  $r_1$  and  $r_2$  relaxivity values were calculated ( $r_1 = 0.05 \text{ mM Gd}^{-1} \cdot \text{s}^{-1}$ ,  $r_2 = 5.3 \text{ mM Gd}^{-1} \cdot \text{s}^{-1}$ ). Notably, the NPs may tend to aggregate in the gel, which may account for the non-linear behaviour; therefore the relaxivities should be interpreted with some caution (Figure 8d). Nevertheless,  $r_2/r_1$  was much greater than 10, therefore, the  $\text{CaF}_2$ : Ce, Gd, Nd NPs could be considered as a  $T_2$  contrast agent [68]. To better investigate the potential biological applications of NPs, we injected NPs subcutaneously into mouse cadavers and found a clear signal at the injection site (Figure 8e). These results indicate that  $\text{CaF}_2$ : Ce, Gd, Nd NPs can be used as MRI contrast agents.



**Figure 8.** In vitro MRI performance of  $\text{CaF}_2$ : Ce, Gd, Nd NPs. (a) Magnetic properties of  $\text{CaF}_2$ : Ce, Gd, Nd NPs; (b) in vitro  $T_1$ -weighted and  $T_2$ -weighted MR images of  $\text{CaF}_2$ : Ce, Gd, Nd NPs at different concentrations in water containing 1% agarose gel; (c) MRI signal intensity of  $\text{CaF}_2$ : Ce, Gd, Nd NPs with increasing repetition time and echo time at different concentrations; (d) in vitro  $T_1$  relaxation rates and  $T_2$  relaxation rates of various Gd concentrations for  $\text{CaF}_2$ : Ce, Gd, Nd NPs; (e) ex vivo MRI images of a mouse cadaver before and after subcutaneous injection of  $\text{CaF}_2$ : Ce, Gd, Nd NPs (10 mg/mL).

#### 4. Conclusions

In summary, we doped  $\text{Ce}^{3+}$ ,  $\text{Gd}^{3+}$  and  $\text{Nd}^{3+}$  into  $\text{CaF}_2$  crystals through a simple hydrothermal process, resulting in the synthesis of  $\text{CaF}_2$ : Ce, Gd, Nd NPs suitable for multimodal imaging. The synthesized NPs were highly pure, and showed low toxicity, good biocompatibility and no immunogenicity.  $\text{CaF}_2$ : Ce, Gd, Nd NPs themselves exhibited dual modes because  $\text{Ce}^{3+}$  and  $\text{Nd}^{3+}$  dopants contribute to NIR-II and PAI, and the presence of  $\text{Gd}^{3+}$  shows a high-contrast  $T_2$  effect for MRI. As such it acts similarly to a super-paramagnetic agent, similar to results obtained for  $\text{Gd}_2\text{O}_3$ -mesoporous silica/gold nanoshells [68]. Therefore,  $\text{CaF}_2$ : Ce, Gd, Nd NPs may be an informative NIR-II/PA/MR multimodal probe for clinical diagnosis. This research also laid the foundation for the use of  $\text{CaF}_2$ : Ce, Gd, Nd NPs for biological imaging of cells and deep tissues.

**Supplementary Materials:** The following supporting information can be downloaded at: <https://www.mdpi.com/article/10.3390/pharmaceutics14122796/s1>, Figure S1: Cell viability. PBMCs were treated with  $\text{CaF}_2$ : Ce, Gd, Nd NPs at varying concentrations (0–125  $\mu\text{g/mL}$ ) on PBMCs for 24 h and 48 h. Data represent the mean values  $\pm$  SD from three independent experiments. Statistical significance was calculated using two-way ANOVA, by comparing experimental groups to control group.

**Author Contributions:** Original data collection and analysis, or interpretation—Z.Y., Y.H. (Yuanyuan He), T.S., K.W., Y.H. (Yang Hao), E.S. and C.E.; writing-original draft—Z.Y.; visualization—Z.Y.; writing-review and editing—Z.Y., H.Z., C.E. and L.J.C.; supervision—C.E. and L.J.C. All authors have read and agreed to the published version of the manuscript.

**Funding:** This work received funding from the European Union's Horizon 2020 research and innovation programme under the Marie Skłodowska Curie grant agreement CANCER (777682), PRISAR2 (872860), ACORN (807281), SIMICA (852985), BIOSAFETY (952520), PAVE (861190), CAST (857894), NOVA-MRI (859908), PIANO (956477). Zhenfeng Yu and Yang Hao received financial support from the China Scholarship Council.

**Institutional Review Board Statement:** This study was performed in line with the principles of the Dutch Animal Ethical Commission with the license of project PE.20.003.013 and approved by the Animal Experimental Committee from the Leiden University Medical Center (LUMC).

**Informed Consent Statement:** Not applicable.

**Data Availability Statement:** Not applicable.

**Acknowledgments:** We appreciate the expertise and access to electron microscopy provided by Roman Koning and Aat Mulder from the Koster lab at LUMC. We also want to express our gratitude to Kaer Labs for their help with the NIR-II imaging. We appreciate Marcel Hesselberth's assistance with SEM and EDX at the Leiden Institute of Physics. We are also appreciative of Anton Lefering of Delft University of Technology for providing the VSM measurements and the preclinical imaging facility for providing the MRI measurements.

**Conflicts of Interest:** The authors declare no conflict of interest.

#### References

1. Yamabe, Y.; Kuroki, Y.; Ishikawa, T.; Miyakawa, K.; Kuroki, S.; Sekiguchi, R. Tumor Staging of Advanced Esophageal Cancer: Combination of Double-Contrast Esophagography and Contrast-Enhanced CT. *Am. J. Roentgenol.* **2008**, *191*, 753–757. [CrossRef] [PubMed]
2. Lind, P.; Kresnik, E.; Kumnig, G.; Gallowitsch, H.-J.; Igerc, I.; Matschnig, S.; Gomez, I.  $^{18}\text{F}$ -FDG-PET in the Follow-up of Thyroid Cancer. *Acta Med. Austriaca* **2003**, *30*, 17–21. [CrossRef] [PubMed]
3. Yun, M.; Kim, W.; Alnafisi, N.; Lacorte, L.; Jang, S.; Alavi, A.  $^{18}\text{F}$ -FDG PET in Characterizing Adrenal Lesions Detected on CT or MRI. *J. Nucl. Med.* **2001**, *42*, 1795–1799. [PubMed]
4. Blend, M.J.; Rohany, M.; Jones-Martinez, N.; De Leon, O.A. Case Study of Tc-99m HMPAO Brain SPECT Imaging in a Patient with Hepatic Encephalopathy and Carotid Artery Stenosis. *Clin. Nucl. Med.* **2010**, *35*, 317–320. [CrossRef]
5. Rocchi, G.; Kasprzak, J.D.; Galema, T.W.; de Jong, N.; Ten Cate, F.J. Usefulness of power Doppler contrast echocardiography to identify reperfusion after acute myocardial infarction. *Am. J. Cardiol.* **2001**, *87*, 278–282. [CrossRef]
6. Gambhir, S.S. Molecular imaging of cancer with positron emission tomography. *Nat. Rev. Cancer* **2002**, *2*, 683–693. [CrossRef]

7. Ziegler, S.I. Positron emission tomography: Principles, technology, and recent developments. *Nucl. Phys. A* **2005**, *752*, 679–687. [\[CrossRef\]](#)
8. Mahmoudi, M.; Serpooshan, V.; Laurent, S. Engineered nanoparticles for biomolecular imaging. *Nanoscale* **2011**, *3*, 3007–3026. [\[CrossRef\]](#)
9. Beekman, F.J.; McElroy, D.P.; Berger, F.; Gambhir, S.S.; Hoffman, E.J.; Cherry, S.R. Towards in vivo nuclear microscopy: Iodine-125 imaging in mice using micro-pinholes. *Eur. J. Nucl. Med. Mol. Imaging* **2002**, *29*, 933–938. [\[CrossRef\]](#)
10. Chatzioannou, A.; Tai, Y.C.; Doshi, N.; Cherry, S.R. Detector development for microPET II: A 1  $\mu$ l resolution PET scanner for small animal imaging. *Phys. Med. Biol.* **2001**, *46*, 2899–2910. [\[CrossRef\]](#)
11. Weissleder, R. A clearer vision for in vivo imaging. *Nat. Biotechnol.* **2001**, *19*, 316–317. [\[CrossRef\]](#)
12. Li, X.; Wang, J.; An, Z.; Yang, M.; Baranov, E.; Jiang, P.; Sun, F.; Moossa, A.R.; Hoffman, R.M. Optically imageable metastatic model of human breast cancer. *Clin. Exp. Metastasis* **2002**, *19*, 347–350. [\[CrossRef\]](#) [\[PubMed\]](#)
13. Hilderbrand, S.A.; Kelly, K.A.; Weissleder, R.; Tung, C.-H. Monofunctional Near-Infrared Fluorochromes for Imaging Applications. *Bioconj. Chem.* **2005**, *16*, 1275–1281. [\[CrossRef\]](#) [\[PubMed\]](#)
14. Wunder, A.; Schellenberger, E.; Mahmood, U.; Bogdanov, A.; Müller-Ladner, U.; Weissleder, R.; Josephson, L. Methotrexate-Induced Accumulation of Fluorescent Annexin V in Collagen-Induced Arthritis. *Mol. Imaging* **2005**, *4*, 15353500200504142. [\[CrossRef\]](#) [\[PubMed\]](#)
15. Arap, W.; Pasqualini, R.; Montalti, M.; Petrizza, L.; Prodi, L.; Rampazzo, E.; Zaccheroni, N.; Marchiò, S. Luminescent silica nanoparticles for cancer diagnosis. *Curr. Med. Chem.* **2013**, *20*, 2195–2211. [\[CrossRef\]](#) [\[PubMed\]](#)
16. Zoetelief, H. Physics for diagnostic radiology, third edition. *Radiat. Prot. Dosim.* **2013**, *154*, 526–529. [\[CrossRef\]](#)
17. Lee, N.; Choi, S.H.; Hyeon, T. Nano-Sized CT Contrast Agents. *Adv. Mater.* **2013**, *25*, 2641–2660. [\[CrossRef\]](#)
18. Debbage, P.; Jaschke, W. Molecular imaging with nanoparticles: Giant roles for dwarf actors. *Histochem. Cell Biol.* **2008**, *130*, 845–875. [\[CrossRef\]](#)
19. Gallo, J.; Long, N.J.; Aboagye, E.O. Magnetic nanoparticles as contrast agents in the diagnosis and treatment of cancer. *Chem. Soc. Rev.* **2013**, *42*, 7816–7833. [\[CrossRef\]](#)
20. Kasban, H.; El-Bendary, M.; Salama, D. A comparative study of medical imaging techniques. *Int. J. Inf. Sci. Intell. Syst.* **2015**, *4*, 37–58.
21. DH, T. Foster FS. In vivo ultrasound biomicroscopy in devel—Opmental biology. *Trends Biotechnol.* **2002**, *20*, S29–S33.
22. Kiessling, F.; Fokong, S.; Bzyl, J.; Lederle, W.; Palmowski, M.; Lammers, T. Recent advances in molecular, multimodal and theranostic ultrasound imaging. *Adv. Drug Deliv. Rev.* **2014**, *72*, 15–27. [\[CrossRef\]](#) [\[PubMed\]](#)
23. Zackrisson, S.; van de Ven, S.M.W.Y.; Gambhir, S.S. Light In and Sound Out: Emerging Translational Strategies for Photoacoustic Imaging. *Cancer Res.* **2014**, *74*, 979–1004. [\[CrossRef\]](#) [\[PubMed\]](#)
24. Eliseeva, S.V.; Bünzli, J.-C.G. Lanthanide luminescence for functional materials and bio-sciences. *Chem. Soc. Rev.* **2010**, *39*, 189–227. [\[CrossRef\]](#)
25. Dong, H.; Du, S.-R.; Zheng, X.-Y.; Lyu, G.-M.; Sun, L.-D.; Li, L.-D.; Zhang, P.-Z.; Zhang, C.; Yan, C.-H. Lanthanide Nanoparticles: From Design toward Bioimaging and Therapy. *Chem. Rev.* **2015**, *115*, 10725–10815. [\[CrossRef\]](#) [\[PubMed\]](#)
26. Yu, Z.; Eich, C.; Cruz, L.J. Recent Advances in Rare-Earth-Doped Nanoparticles for NIR-II Imaging and Cancer Theranostics. *Front. Chem.* **2020**, *8*. [\[CrossRef\]](#) [\[PubMed\]](#)
27. Bünzli, J.-C.G.; Piguet, C. Taking advantage of luminescent lanthanide ions. *Chem. Soc. Rev.* **2005**, *34*, 1048–1077. [\[CrossRef\]](#) [\[PubMed\]](#)
28. Pokhrel, M.; Mimun, L.C.; Yust, B.; Kumar, G.A.; Dhanale, A.; Tang, L.; Sardar, D.K. Stokes emission in GdF<sub>3</sub>:Nd<sup>3+</sup> nanoparticles for bioimaging probes. *Nanoscale* **2014**, *6*, 1667–1674. [\[CrossRef\]](#)
29. Qin, Q.-S.; Zhang, P.-Z.; Sun, L.-D.; Shi, S.; Chen, N.-X.; Dong, H.; Zheng, X.-Y.; Li, L.-M.; Yan, C.-H. Ultralow-power near-infrared excited neodymium-doped nanoparticles for long-term in vivo bioimaging. *Nanoscale* **2017**, *9*, 4660–4664. [\[CrossRef\]](#)
30. Wang, Y.-F.; Liu, G.-Y.; Sun, L.-D.; Xiao, J.-W.; Zhou, J.-C.; Yan, C.-H. Nd<sup>3+</sup>-Sensitized Upconversion Nanophosphors: Efficient In Vivo Bioimaging Probes with Minimized Heating Effect. *ACS Nano* **2013**, *7*, 7200–7206. [\[CrossRef\]](#)
31. Cao, C.; Liu, Q.; Shi, M.; Feng, W.; Li, F. Lanthanide-Doped Nanoparticles with Upconversion and Downshifting Near-Infrared Luminescence for Bioimaging. *Inorg. Chem.* **2019**, *58*, 9351–9357. [\[CrossRef\]](#)
32. Tiwari, S.P.; Maurya, S.K.; Yadav, R.S.; Kumar, A.; Kumar, V.; Joubert, M.-F.; Swart, H.C. Future prospects of fluoride based upconversion nanoparticles for emerging applications in biomedical and energy harvesting. *J. Vac. Sci. Technol. B* **2018**, *36*, 060801. [\[CrossRef\]](#)
33. Dubey, V.; Som, S.; Kumar, V. *Luminescent Materials in Display and Biomedical Applications*; CRC Press, Taylor & Francis Group: Boca Raton, FL, USA, 2021.
34. Falcony, C.; Aguilar-Frutis, M.A.; García-Hipólito, M. Spray Pyrolysis Technique; High-K Dielectric Films and Luminescent Materials: A Review. *Micromachines* **2018**, *9*, 414. [\[CrossRef\]](#) [\[PubMed\]](#)
35. Grzeszkiewicz, K.; Marciniak, L.; Stręk, W.; Hreniak, D. Downconversion in Y<sub>2</sub>Si<sub>2</sub>O<sub>7</sub>: Pr<sup>3+</sup>, Yb<sup>3+</sup> polymorphs for its possible application as luminescent concentrators in photovoltaic solar-cells. *J. Lumin.* **2016**, *177*, 172–177. [\[CrossRef\]](#)
36. Tan, J.; Jin, X. Monodisperse, colloidal and luminescent calcium fluoride nanoparticles via a citrate-assisted hydrothermal route. *J. Colloid Interface Sci.* **2018**, *531*, 444–450. [\[CrossRef\]](#) [\[PubMed\]](#)
37. Cortelletti, P.; Facciotti, C.; Cantarelli, I.X.; Canton, P.; Quintanilla, M.; Vetrone, F.; Speghini, A.; Pedroni, M. Nd<sup>3+</sup> activated CaF<sub>2</sub> NPs as colloidal nanothermometers in the biological window. *Opt. Mater.* **2017**, *68*, 29–34. [\[CrossRef\]](#)

38. Su, L.; Xu, J.; Li, H.; Wen, L.; Yang, W.; Zhao, Z.; Si, J.; Dong, Y.; Zhou, G. Crystal growth and spectroscopic characterization of Yb-doped and Yb, Na-codoped  $\text{CaF}_2$  laser crystals by TGT. *J. Cryst. Growth* **2005**, *277*, 264–268. [\[CrossRef\]](#)
39. Gao, X.; Fang, G.; Wang, Y.; Zhu, Z.; You, Z.; Li, J.; Sun, Y.; Tu, C. Visible and mid-infrared spectral performances of  $\text{Dy}^{3+}$ :  $\text{CaF}_2$  and  $\text{Dy}^{3+}/\text{Y}^{3+}$ :  $\text{CaF}_2$  crystals. *J. Alloys Compd.* **2021**, *856*, 158083. [\[CrossRef\]](#)
40. Cortelletti, P.; Pedroni, M.; Boschi, F.; Pin, S.; Ghigna, P.; Canton, P.; Vetrone, F.; Speghini, A. Luminescence of  $\text{Eu}^{3+}$  Activated  $\text{CaF}_2$  and  $\text{SrF}_2$  Nanoparticles: Effect of the Particle Size and Codoping with Alkaline Ions. *Cryst. Growth Des.* **2018**, *18*, 686–694. [\[CrossRef\]](#)
41. Xu, B.; Li, D.; Huang, Z.; Tang, C.; Mo, W.; Ma, Y. Alleviating luminescence concentration quenching in lanthanide doped  $\text{CaF}_2$  based nanoparticles through  $\text{Na}^+$  ion doping. *Dalton Trans.* **2018**, *47*, 7534–7540. [\[CrossRef\]](#)
42. Serrano, D.; Braud, A.; Doualan, J.L.; Camy, P.; Moncorgé, R.  $\text{Pr}^{3+}$  cluster management in  $\text{CaF}_2$  by codoping with  $\text{Lu}^{3+}$  or  $\text{Yb}^{3+}$  for visible lasers and quantum down-converters. *J. Opt. Soc. Am. B* **2012**, *29*, 1854–1862. [\[CrossRef\]](#)
43. Yu, H.; Su, L.; Qian, X.; Jiang, D.; Wu, Q.; Tang, F.; Wang, J.; Xu, J. Influence of  $\text{Gd}^{3+}$  on the Optical Properties of  $\text{Dy}^{3+}$ -Activated  $\text{CaF}_2$  Single Crystal for White LED Application. *J. Electron. Mater.* **2019**, *48*, 2910–2915. [\[CrossRef\]](#)
44. Normani, S.; Braud, A.; Soulard, R.; Doualan, J.L.; Benayad, A.; Menard, V.; Brasse, G.; Moncorgé, R.; Goossens, J.P.; Camy, P. Site selective analysis of  $\text{Nd}^{3+}$ – $\text{Lu}^{3+}$  codoped  $\text{CaF}_2$  laser crystals. *CrystEngComm* **2016**, *16*, 9016–9025. [\[CrossRef\]](#)
45. Zhang, Z.; Wang, S.; Feng, X.; Wu, Q.; Qian, X.; Wu, A.; Liu, J.; Mei, B.; Su, L. Growth, Characterization, and Efficient Continuous-Wave Laser Operation in Nd, Gd:  $\text{CaF}_2$  Single-Crystal Fibers. *Cryst. Growth Des.* **2020**, *20*, 6329–6336. [\[CrossRef\]](#)
46. Yu, Z.; He, Y.; Schomann, T.; Wu, K.; Hao, Y.; Suidgeest, E.; Zhang, H.; Eich, C.; Cruz, L.J. Achieving Effective Multimodal Imaging with Rare-Earth Ion-Doped  $\text{CaF}_2$  Nanoparticles. *Pharmaceutics* **2022**, *14*, 840. [\[CrossRef\]](#) [\[PubMed\]](#)
47. Wang, T.; Yu, Y.; Ji, X.; Xu, W.; Fu, Y.; Cao, H.; He, Q.; Cheng, J. A new method to synthesize Sub-10 nm  $\text{CaF}_2$ :  $\text{Nd}^{3+}$  nanoparticles and fluorescent enhancement via  $\text{Li}^+$  ions or  $\text{Ce}^{3+}$  ions doping. *Dyes Pigments* **2020**, *175*, 108129. [\[CrossRef\]](#)
48. Ni, D.; Zhang, J.; Wang, J.; Hu, P.; Jin, Y.; Tang, Z.; Yao, Z.; Bu, W.; Shi, J. Oxygen vacancy enables markedly enhanced magnetic resonance imaging-guided photothermal therapy of a  $\text{Gd}^{3+}$ -doped contrast agent. *ACS Nano* **2017**, *11*, 4256–4264. [\[CrossRef\]](#) [\[PubMed\]](#)
49. Rajendran, D.; Elizabeth, J.; Manoharan, S.; Vellala, N.; Kootallur, B.; Paul, P.M.; Angamuthu, A.; Bhagavathsingh, J. Synthesis, Characterization and Relaxivity Validations of Gd (III) Complex of DOTA Tetrahydrazide as MRI Contrast Agent. *J. Mol. Struct.* **2022**, 132474. [\[CrossRef\]](#)
50. Pedroni, M.; Piccinelli, F.; Passuello, T.; Polizzi, S.; Ueda, J.; Haro-González, P.; Martinez Maestro, L.; Jaque, D.; García-Solé, J.; Bettinelli, M.; et al. Water ( $\text{H}_2\text{O}$  and  $\text{D}_2\text{O}$ ) Dispersible NIR-to-NIR Upconverting  $\text{Yb}^{3+}/\text{Tm}^{3+}$  Doped  $\text{MF}_2$  ( $\text{M} = \text{Ca}, \text{Sr}$ ) Colloids: Influence of the Host Crystal. *Cryst. Growth Des.* **2013**, *13*, 4906–4913. [\[CrossRef\]](#)
51. De Anda, J.; Huerta, E.F.; Balderas, J.U.; Righini, G.C.; Falcony, C. The effect of  $\text{Li}^+$  incorporation in  $\text{Yb}^{3+}$ - $\text{Nd}^{3+}$  co-doped  $\text{CaF}_2$  phosphors over the NIR photoluminescence emission excited under visible light. *Ceram. Int.* **2021**, *47*, 4694–4701. [\[CrossRef\]](#)
52. Yu, Z.-f.; Shi, J.-p.; Li, J.-l.; Li, P.-h.; Zhang, H.-w. Luminescence enhancement of  $\text{CaF}_2$ : $\text{Nd}^{3+}$  nanoparticles in the second near-infrared window for in vivo imaging through  $\text{Y}^{3+}$  doping. *J. Mater. Chem. B* **2018**, *6*, 1238–1243. [\[CrossRef\]](#)
53. Li, X.; Hao, Q.; Jiang, D.; Wu, Q.; Zhang, Z.; Zhang, Z.; Liu, J.; Su, L. Smooth and flat photoluminescence spectra of  $\text{Nd}^{3+}$  active ions in tri-doped  $\text{CaF}_2$  single crystals. *Opt. Mater. Express* **2020**, *10*, 704–714. [\[CrossRef\]](#)
54. Sasidharan, S.; Jayasree, A.; Fazal, S.; Koyakutty, M.; Nair, S.V.; Menon, D. Ambient temperature synthesis of citrate stabilized and biofunctionalized, fluorescent calcium fluoride nanocrystals for targeted labeling of cancer cells. *Biomater. Sci.* **2013**, *1*, 294–305. [\[CrossRef\]](#) [\[PubMed\]](#)
55. Varga, Z.; Fehér, B.; Kitka, D.; Wacha, A.; Bóta, A.; Berényi, S.; Pipich, V.; Fraikin, J.-L. Size measurement of extracellular vesicles and synthetic liposomes: The impact of the hydration shell and the protein corona. *Colloids Surf. B Biointerfaces* **2020**, *192*, 111053. [\[CrossRef\]](#) [\[PubMed\]](#)
56. Wang, S.; Jiang, D.; Wu, Q.; Pang, S.; Wang, J.; Qian, X.; Liu, J.; Mei, B.; Su, L. Spectral properties and highly efficient continuous-wave laser operation in Nd, Gd:  $\text{CaF}_2$  crystals. *J. Alloys Compd.* **2019**, *781*, 629–632. [\[CrossRef\]](#)
57. Serqueira, E.O.; Dantas, N.O.; Monte, A.F.G.; Bell, M.J.V. Judd Ofelt calculation of quantum efficiencies and branching ratios of  $\text{Nd}^{3+}$  doped glasses. *J. Non-Cryst. Solids* **2006**, *352*, 3628–3632. [\[CrossRef\]](#)
58. De la Rosa-Cruz, E.; Kumar, G.A.; Diaz-Torres, L.A.; Martínez, A.; Barbosa-García, O. Spectroscopic characterization of  $\text{Nd}^{3+}$  ions in barium fluoroborophosphate glasses. *Opt. Mater.* **2001**, *18*, 321–329. [\[CrossRef\]](#)
59. Turri, G.; Webster, S.; Bass, M.; Toncelli, A. Temperature-Dependent Stimulated Emission Cross-Section in  $\text{Nd}^{3+}$ : YLF Crystal. *Materials* **2021**, *14*, 431. [\[CrossRef\]](#)
60. Fornaguera, C.; Calderó, G.; Mitjans, M.; Vinardell, M.P.; Solans, C.; Vauthier, C. Interactions of PLGA nanoparticles with blood components: Protein adsorption, coagulation, activation of the complement system and hemolysis studies. *Nanoscale* **2015**, *7*, 6045–6058. [\[CrossRef\]](#)
61. Alkahtani, M.; Alsofyani, N.; Alfahd, A.; Almughim, A.A.; Almughem, F.A.; Alshehri, A.A.; Qasem, H.; Hemmer, P.R. Engineering Red-Enhanced and Biocompatible Upconversion Nanoparticles. *Nanomaterials* **2021**, *11*, 284. [\[CrossRef\]](#)
62. Villadangos, J.A.; Cardoso, M.A.; Steptoe, R.J.; van Berkel, D.; Pooley, J.; Carbone, F.R.; Shortman, K. MHC Class II Expression Is Regulated in Dendritic Cells Independently of Invariant Chain Degradation. *Immunity* **2001**, *14*, 739–749. [\[CrossRef\]](#)

- 
63. Cruz, L.J.; Rosalia, R.A.; Kleinovink, J.W.; Rueda, F.; Löwik, C.W.G.M.; Ossendorp, F. Targeting nanoparticles to CD40, DEC-205 or CD11c molecules on dendritic cells for efficient CD8<sup>+</sup> T cell response: A comparative study. *J. Control. Release* **2014**, *192*, 209–218. [[CrossRef](#)] [[PubMed](#)]
  64. Minns, D.; Smith, K.J.; Findlay, E.G. Orchestration of adaptive T cell responses by neutrophil granule contents. *Mediat. Inflamm.* **2019**, *2019*, 8968943. [[CrossRef](#)] [[PubMed](#)]
  65. Sheng, Y.; Liao, L.-D.; Bandla, A.; Liu, Y.-H.; Yuan, J.; Thakor, N.; Tan, M.C. Enhanced near-infrared photoacoustic imaging of silica-coated rare-earth doped nanoparticles. *Mater. Sci. Eng. C* **2017**, *70*, 340–346. [[CrossRef](#)] [[PubMed](#)]
  66. Visscher, M.; Pouw, J.J.; van Baarlen, J.; Klaase, J.M.; Ten Haken, B. Quantitative analysis of superparamagnetic contrast agent in sentinel lymph nodes using ex vivo vibrating sample magnetometry. *IEEE Trans. Biomed. Eng.* **2013**, *60*, 2594–2602. [[CrossRef](#)] [[PubMed](#)]
  67. Yang, W.; Zhang, Z.; Zhang, X.; Wang, X.; Jiang, X.; Leng, Z.; Lin, H.; Zeng, F.; Li, C.; Su, Z. Enhancement of fluorescence and magnetic properties of CeF<sub>3</sub>: RE<sup>3+</sup> (Tb, Gd) nanoparticles via multi-band UV excitation and Li doping regulation. *Ceram. Int.* **2021**, *47*, 16450–16459. [[CrossRef](#)]
  68. Kadria-Vili, Y.; Neumann, O.; Zhao, Y.; Nordlander, P.; Martinez, G.V.; Bankson, J.A.; Halas, N.J. Gd<sub>2</sub>O<sub>3</sub>-mesoporous silica/gold nanoshells: A potential dual T<sub>1</sub>/T<sub>2</sub> contrast agent for MRI-guided localized near-IR photothermal therapy. *Proc. Natl. Acad. Sci. USA* **2022**, *119*, e2123527119.